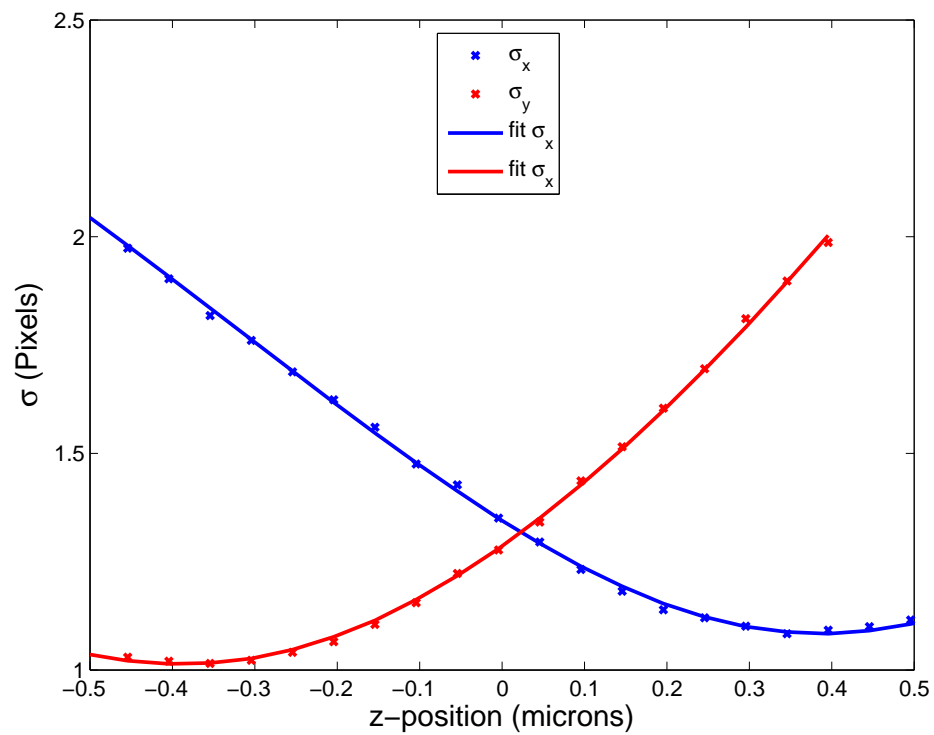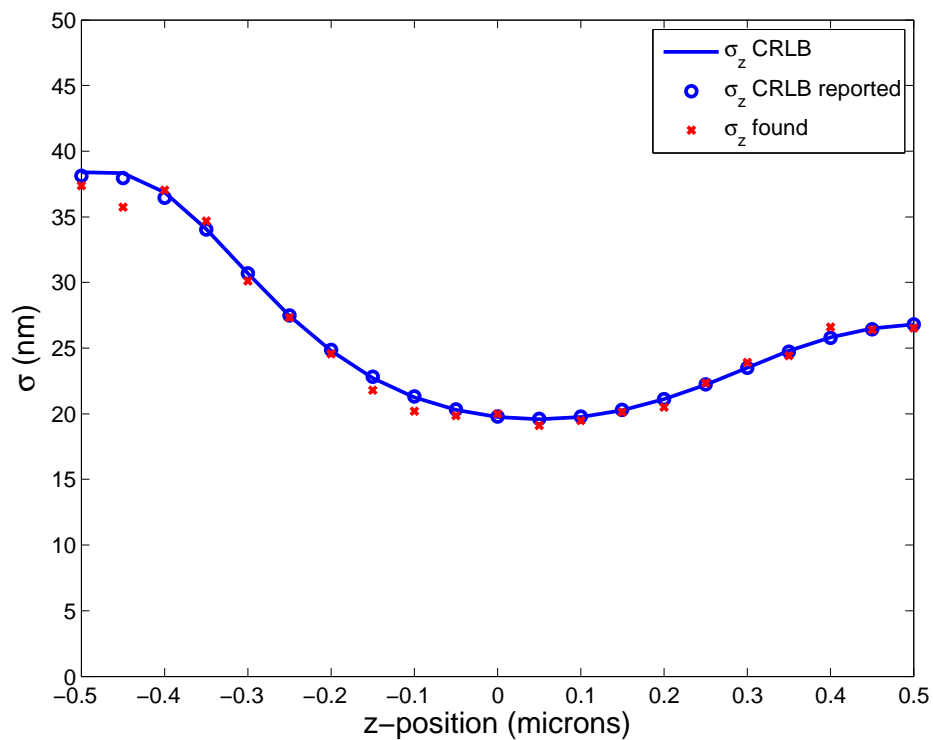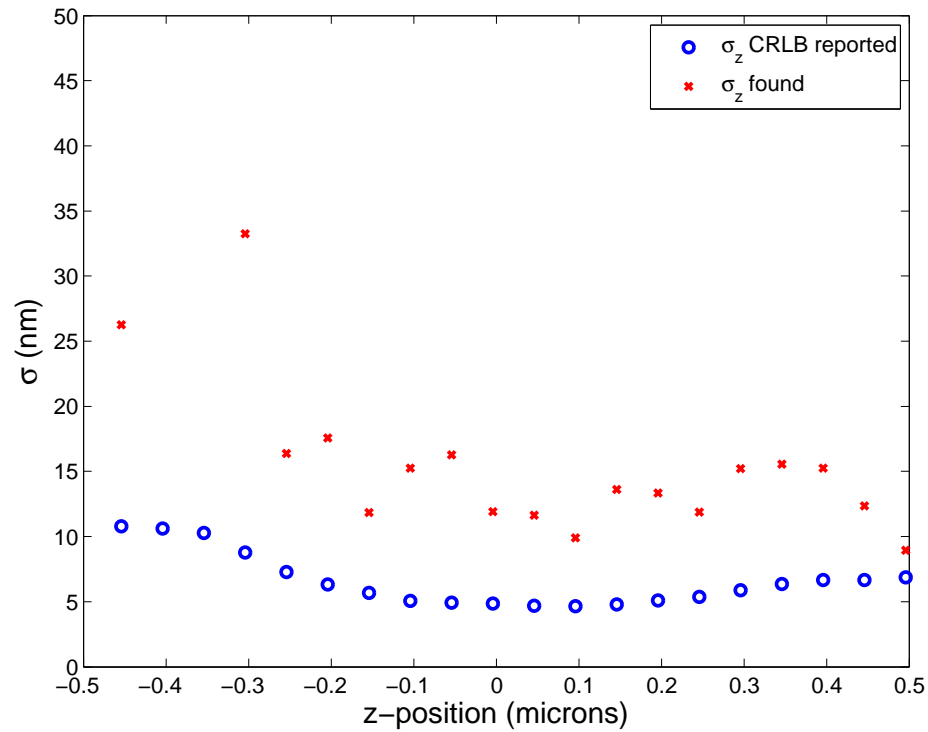**Supplementary Figure 1**

Supplementary Figure 1. Fitting $\sigma_x(z)$ and $\sigma_y(z)$ to the astigmatic model of the PSF. Beads were used as calibration markers which were moved in steps of 50 nm by a piezo stage.

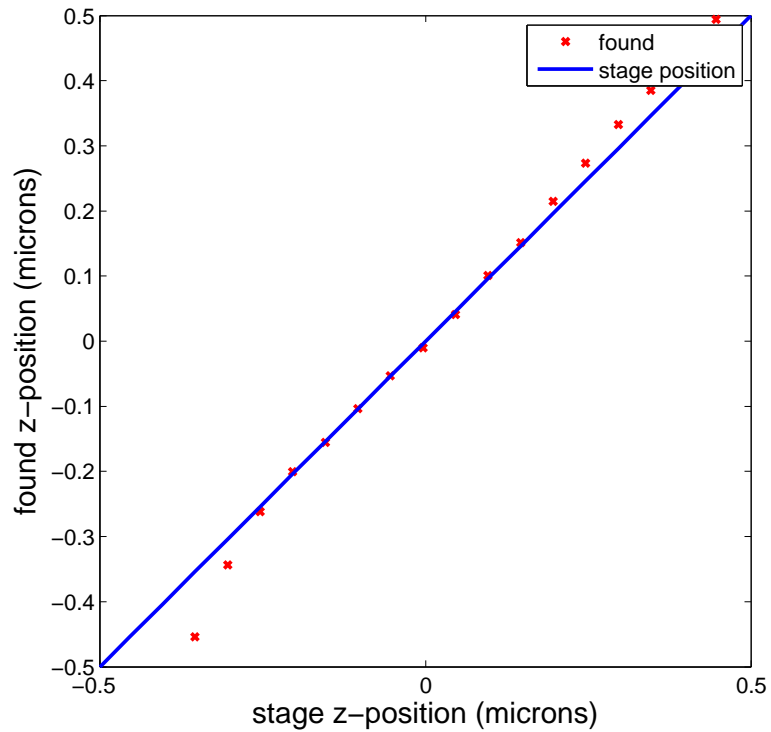**Supplementary Figure 2**

Supplementary Figure 2. Simultaneous fits to x, y, z, the emission and background rates synthetic data. Shown is only the precision in z. The reported values of the CRLB of the algorithm are shown as circles whereas the found standard deviation is indicated with crosses.

Supplementary Figure 3

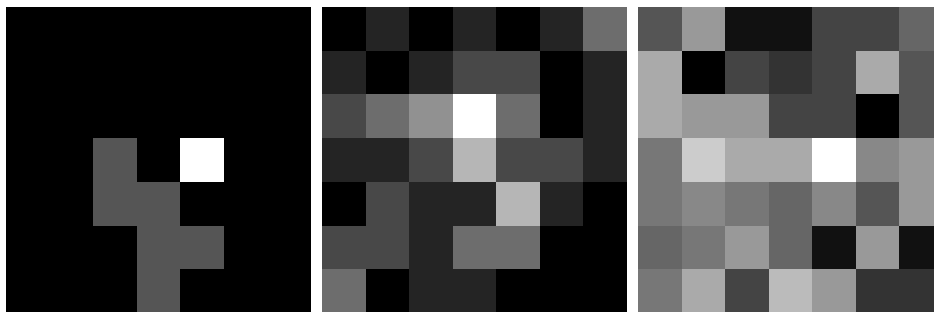**Supplementary Figure 3.** The standard deviation of found z-positions. Found standard deviations do not match that reported from CRLB calculations because of aberrations present in experimental images that are not accounted for in the imaging model.

Supplementary Figure 4

Supplementary Figure 4. Experimental bead data. Estimated z-positions versus piezo stage z position. The line has slope one.

Supplementary Figure 5. Example images of simulated single molecules with emission and background rates (in photons) that corresponds with the $\sigma_{PSF}/2$ border. Here the iterative method is still able to both estimate the CRLB and find the position with CRLB accuracy. We show a 7×7 area with $\sigma_{PSF} = 1$. From left to right: background rates 0, 1 and 10. The shown photon counts are 10, 30 and 50.

Supplementary Figure 6
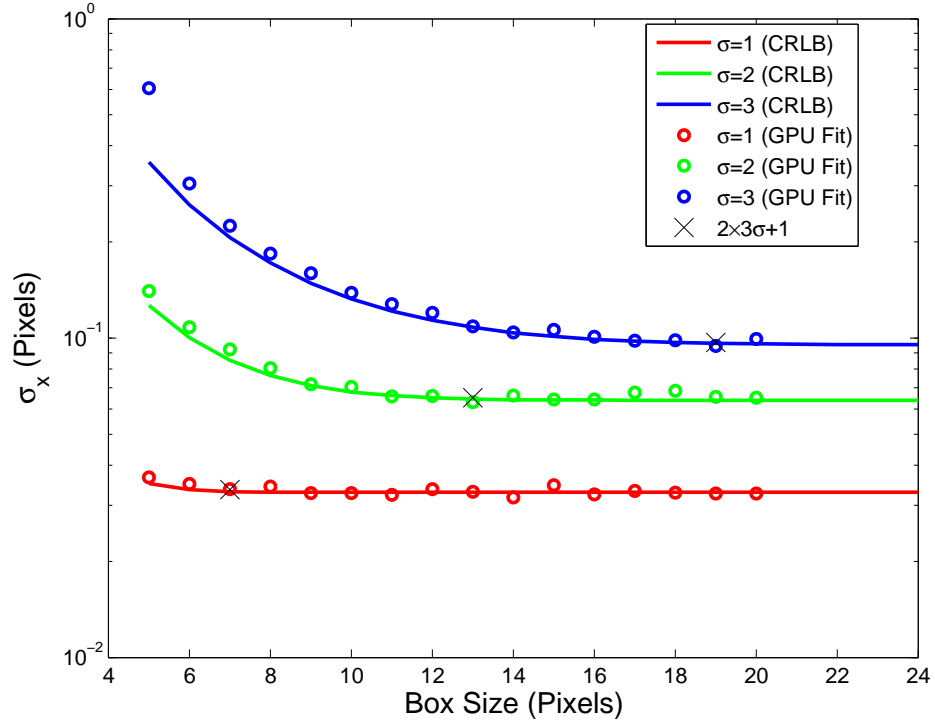
Supplementary Figure 6. Localization Accuracy versus Fit Region Size. The best localization accuracy is calculated using the CRLB and compared to the standard deviation of x-position error in simulated data stacks for $I_0 = 1000$ and $bg = 0$. The improvement of localization accuracy diminishes beyond a linear box size of $(2 \times 3\sigma + 1)$.

Supplementary Figure 7
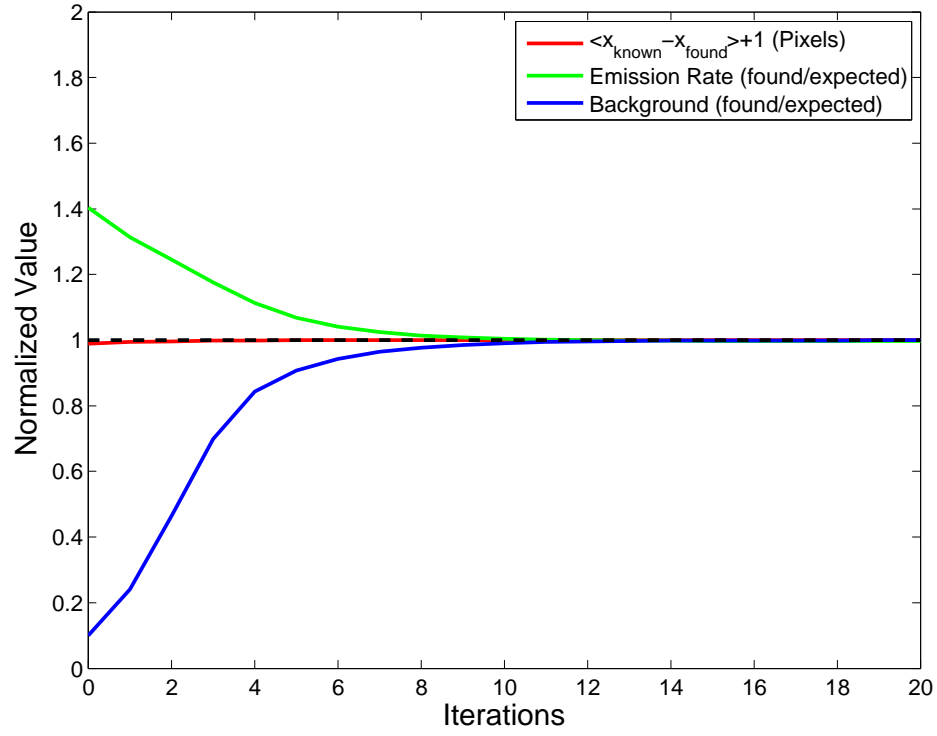
Supplementary Figure 7. Convergence of the Iterative Method. The convergence of position (red) intensity (green) and background rate (blue) to known, correct values are shown. Calculation were made using $\sigma_{PSF} = 3$ and a square fitting region of linear size and $2 \times 3\sigma_{PSF} + 1 = 19$, which represents the slowest convergence of any combination of σ_{PSF} and box size used.

Supplementary Figure 8
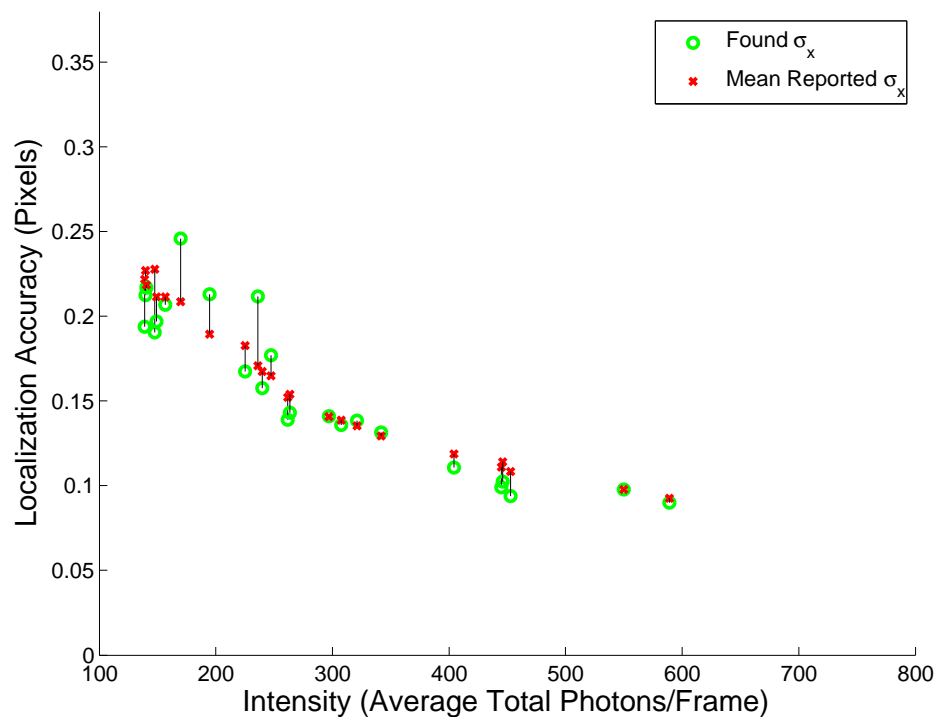
Supplementary Figure 8. Analysis of Single Molecule Experiments. The standard deviation of the x-positions found in repeated measurements of single, immobilized Cy5 molecules (green) are compared with the average accuracy calculated frame by frame using the CRLB (red). Found background rates (not shown) vary between single molecules giving a range of possible localization accuracy values for each intensity.

Supplementary Table 1

Processor	Total Time	Segmentation	ROI collection	Fitting	Reconstruction
		10^4 frames, 10^5 localizations			
GPU	8.8 s	90 %	1 %	8.5 %	0.5 %
CPU	41 s	19.4 %	0.2 %	80.3 %	0.1 %
		10^4 frames, 10^6 localizations			
GPU	14 s	57.8 %	2.7 %	38.9 %	0.6 %
CPU	300 s	2.8 %	0.1 %	97 %	0.1 %

Supplementary Table 1. Comparison of total processing time for 10,000 frames of 128x128 pixels. Fitting corresponds to σ_{PSF}=1 and 7×7 pixel fitting areas.

Supplementary Note

The Image Formation Model

In the paraxial limit, the microscope point spread function (PSF) can be taken as the Airy pattern $\text{PSF}(r) = \frac{J_1(\alpha r)^2}{(\alpha r)^2}$, where $\alpha = \frac{2\pi \text{NA}}{\lambda}$ and J_1 is the Bessel function of first kind. However, in fluorescence microscopy, objective lenses with numerical apertures (NAs) of 1.2 or greater are most often used when imaging single fluorescent molecules in order to collect as many emitted photons as possible; the collection efficiency is $\propto \text{NA}^2$. A proper calculation of PSFs for these high NA objectives must include vectorial effects, aberrations in the optical system and apodization in the objective lens [1, 2]. In lieu of such a detailed measurement and description of the PSF, often a two-dimensional Gaussian shape is used as a compact and good expression of the PSF [3]. We use the two-dimensional Gaussian approximation of the PSF to greatly simplify the proceeding analysis. This also holds for extension to 3D confocal laser scanning PSFs [3]. The simplified form of the PSF is then

$$\text{PSF}(x,y) = \frac{1}{2\pi\sigma^2} e^{\frac{-(x-\theta_x)^2 - (y-\theta_y)^2}{2\sigma^2}} , \tag{1}$$

where $\theta_{x,y}$ is the position of the emitter. PSF approximations also often neglect the finite size of the detector pixels. In this work, the imaging model, denoted by $\mu_k(x,y)$, will always include the integration over finite pixels which is given by:

$$\mu_k(x,y) = \theta_{I_0} \int_{A_k} \text{PSF}(u,v) \mathrm{d}u\mathrm{d}v + \theta_{bg} , \tag{2}$$

where $\mu_k(x,y)$ denotes the expected value in the kth pixel, θ_{bg} the expected background count, θ_{I_0} the expected photon count and the integral is over the finite area A_k of the kth pixel, which is centered at (x,y). The Gaussian approximation allows the results to be expressed in terms of error functions (which simplify the implementation as they are supported in CUDA [4]). If we assume uniform pixels with unit size, the imaging model is given as:

$$\mu_k(x,y) = \theta_{I_0} \Delta\text{E}_x(x,y)\Delta\text{E}_y(x,y) + \theta_{bg} , \tag{3}$$

where the expressions

$$\Delta\text{E}_x(x,y) \equiv \frac{1}{2}\text{erf}\left(\frac{x - \theta_x + \frac{1}{2}}{2\sigma^2}\right) - \frac{1}{2}\text{erf}\left(\frac{x - \theta_x - \frac{1}{2}}{2\sigma^2}\right) , \tag{4a}$$

$$\Delta\text{E}_y(x,y) \equiv \frac{1}{2}\text{erf}\left(\frac{y - \theta_y + \frac{1}{2}}{2\sigma^2}\right) - \frac{1}{2}\text{erf}\left(\frac{y - \theta_y - \frac{1}{2}}{2\sigma^2}\right) , \tag{4b}$$

are used to shorten notation. The Gaussian standard deviation, σ, is determined in practice by fitting to images of small beads or single molecules under the operating conditions of the microscope. It can also be computed directly from a theoretical PSF and its FHWM [3]. Eq. 3 will be used as the imaging model for the parameter estimation in the following.

Cramér Rao Lower Bound

The Cramér Rao Lower Bound (CRLB) is the limiting lower bound of the variance for any unbiased parameter estimator [5]. The general expression for the CRLB is given by the inverse of the Fisher information matrix

$$var(\hat{\theta}) \geq I(\theta)^{-1} , \tag{5}$$

where $var(\hat{\theta})$ is the variance of an estimator and $I(\theta)$ is the Fisher information matrix. The equal sign is the minimum of that estimation and is referred to as the CRLB.

The Fisher Information Matrix for the imaging model μ

The elements of the Fisher information matrix are given by the expectation of the log-likelihood:

$$I_{ij}(\theta) = E\left[\frac{\partial \ln(L(\vec{x}|\theta))}{\partial \theta_i}\frac{\partial \ln(L(\vec{x}|\theta))}{\partial \theta_j}\right], \tag{6}$$

where θ is the set of parameters being estimated $\theta = [\theta_1...\theta_N]$ and $L(\vec{x}|\theta)$ is the likelihood of the data set $\vec{x}$ given the model generated by θ. Here the parameters are $\theta = [\theta_x, \theta_y, \theta_{I_0}, \theta_{bg}]$. For a Poisson process the likelihood is given by

$$L(\vec{x}|\theta) = \prod_k \frac{\mu_k(x,y)^{x_k}e^{-\mu_k(x,y)}}{x_k!}. \tag{7}$$

Using Eq. 6, Eq. 7 and the Stirling approximation ($\ln n! \approx n \ln n - n$ for large n) it is straightforward to show that

$$I_{ij}(\theta) = E\left[\sum_k (x_k - \mu_k(x,y))^2 \frac{1}{\mu_k(x,y)^2}\frac{\partial \mu_k(x,y)}{\partial \theta_i}\frac{\partial \mu_k(x,y)}{\partial \theta_j}\right]. \tag{8}$$

Using the fact that $(x_k - \mu_k(x,y))^2$ is the variance and equal to the expected value for a Poisson process, we obtain

$$I_{ij}(\theta) = \sum_k \frac{1}{\mu_k(x,y)}\frac{\partial \mu_k(x,y)}{\partial \theta_i}\frac{\partial \mu_k(x,y)}{\partial \theta_j}. \tag{9}$$

The partial derivatives with respect to the parameters are given by

$$\frac{\partial \mu_k(x,y)}{\partial \theta_x} = \frac{\theta_{I_0}}{2\sigma^2}\int_{A_k}(\theta_x - u)\text{PSF}(u,v)\mathrm{d}u\mathrm{d}v \tag{10a}$$

$$\frac{\partial \mu_k(x,y)}{\partial \theta_y} = \frac{\theta_{I_0}}{2\sigma^2}\int_{A_k}(\theta_y - v)\text{PSF}(u,v)\mathrm{d}u\mathrm{d}v \tag{10b}$$

$$\frac{\partial \mu_k(x,y)}{\partial \theta_{I_0}} = \int_{A_k}\text{PSF}(u,v)\mathrm{d}u\mathrm{d}v \tag{10c}$$

$$\frac{\partial \mu_k(x,y)}{\partial \theta_{bg}} = 1, \tag{10d}$$

which upon performing the integration become

$$\frac{\partial \mu_k(x,y)}{\partial \theta_x} = \frac{\theta_{I_0}}{\sqrt{2\pi}\sigma}\left(e^{\frac{-(x_k - \theta_x - \frac{1}{2})^2}{2\sigma^2}} - e^{\frac{-(x_k - \theta_x + \frac{1}{2})^2}{2\sigma^2}}\right)\Delta\text{E}_y(x,y) \tag{11a}$$

$$\frac{\partial \mu_k(x,y)}{\partial \theta_y} = \frac{\theta_{I_0}}{\sqrt{2\pi}\sigma}\left(e^{\frac{-(y_k - \theta_y - \frac{1}{2})^2}{2\sigma^2}} - e^{\frac{-(y_k - \theta_y + \frac{1}{2})^2}{2\sigma^2}}\right)\Delta\text{E}_x(x,y) \tag{11b}$$

$$\frac{\partial \mu_k(x,y)}{\partial \theta_{I_0}} = \Delta\text{E}_x(x,y)\Delta\text{E}_y(x,y) \tag{11c}$$

$$\frac{\partial \mu_k(x,y)}{\partial \theta_{bg}} = 1. \tag{11d}$$

Note that Eq. 9 is general, whereas the Gaussian PSF model allows the simple expressions in Eqs. 10 and 11. Simultaneous fitting of the position, intensity and background leads to off-diagonal elements in $I(\theta)$. The CRLBs for the estimation of θ are equal to the diagonal elements of the matrix inversion of $I(\theta)$, i.e. $var(\theta_i) = (I^{-1})_{ii}$.

Iterative Method

We employ essentially a Newton-Raphson method [6] to find the parameters θ that maximize $\ln(L(\vec{x}|\theta))$. This is equal to the maximum likelihood estimate of the parameters $\theta_{ML} = \arg\max_{\theta} L(\vec{x}|\theta)$. The derivatives required for the iterative updates are calculated in a straightforward manner from Eq. 7

$$\frac{\partial \ln(L(\vec{x}|\theta))}{\partial \theta_i} = \sum_k \frac{\partial \mu_k(x,y)}{\partial \theta_i} \left(\frac{x_k}{\mu_k(x,y)} - 1 \right) . \tag{12}$$

Given an adequate guess of starting parameters, the parameters are updated according to:

$$\theta_i \to \theta_i + \left[\sum_k \frac{\partial \mu_k(x,y)}{\partial \theta_i} \left(\frac{x_k}{\mu_k(x,y)} - 1 \right) \right] \times$$
$$\left[\sum_k \frac{\partial^2 \mu_k(x,y)}{\partial \theta_i^2} \left(\frac{x_k}{\mu_k(x,y)} - 1 \right) - \frac{\partial \mu_k(x,y)}{\partial \theta_i}^2 \frac{x_k}{\mu_k(x,y)^2} \right]^{-1} . \tag{13}$$

The first derivatives are given in the previous section, (see Eqs 11) and the second derivatives are given by

$$\frac{\partial^2 \mu_k(x,y)}{\partial \theta_x^2} = \frac{\theta_{I_0}}{\sqrt{2\pi}\sigma^3} \left((x_k - \theta_x - \tfrac{1}{2})e^{\frac{-(x_k - \theta_x - \frac{1}{2})^2}{2\sigma^2}} - (x_k - \theta_x + \tfrac{1}{2})e^{\frac{-(x_k - \theta_x + \frac{1}{2})^2}{2\sigma^2}} \right) \Delta E_y(x,y) , \tag{14a}$$

$$\frac{\partial^2 \mu_k(x,y)}{\partial \theta_y^2} = \frac{\theta_{I_0}}{\sqrt{2\pi}\sigma^3} \left((y_k - \theta_y - \tfrac{1}{2})e^{\frac{-(y_k - \theta_y - \frac{1}{2})^2}{2\sigma^2}} - (y_k - \theta_y + \tfrac{1}{2})e^{\frac{-(y_k - \theta_y + \frac{1}{2})^2}{2\sigma^2}} \right) \Delta E_x(x,y) , \tag{14b}$$

$$\frac{\partial^2 \mu_k(x,y)}{\partial \theta_{\theta_{I_0}}^2} = \frac{\partial^2 \mu_k(x,y)}{\partial \theta_{bg}^2} = 0 . \tag{14c}$$

Extension to 3D Astigmatic Imaging

Following Holtzer [7] and using σ_0 as usual the PSF near focus can be described by a 2D Gaussian with a z-dependent standard deviation

$$\sigma(z) = \sigma_0 \sqrt{1 + \frac{z^2}{d^2} + A\frac{z^3}{d^2} + B\frac{z^4}{d^2}} , \tag{15}$$

where σ_0 is the in focus standard deviation, d is the depth of focus (a constant for a particular objective), A and B are empirical constants ($B \approx 0$ for our experiments, see Results). Introducing an elliptical lens in the beam path splits the focal plane into two perpendicular focal planes at different depth giving an asymmetric PSF. The form of the PSF on the detector is then approximated by

$$\text{PSF}(x,y) = \frac{1}{2\pi\sigma_x(\theta_z)\sigma_y(\theta_z)} e^{-\frac{(x-\theta_x)^2}{2\sigma_x(\theta_z)^2} - \frac{(y-\theta_y)^2}{2\sigma_y(\theta_z)^2}} , \tag{16}$$

where $\theta_{x,y,z}$ is the position of the emitter. Half way between the two focal planes we have (assuming Gaussian optics at the disk of least confusion) $\sigma_x = \sigma_y$ and $\sigma_x, \sigma_y \geq \sigma_0$; here we define $z = 0$. Focal planes for each direction are above and below $z = 0$. Assuming the x-direction is focused above and using Eq. 15, $z \to z - \gamma$ for the x-direction, $z \to z + \gamma$ for the y-direction

$$\sigma_x(z) = \sigma_{0x} \sqrt{1 + \frac{(z-\gamma)^2}{d^2} + A_x\frac{(z-\gamma)^3}{d^2} + B_x\frac{(z-\gamma)^4}{d^2}} , \tag{17a}$$

$$\sigma_y(z) = \sigma_{0y} \sqrt{1 + \frac{(z+\gamma)^2}{d^2} + A_y\frac{(z+\gamma)^3}{d^2} + B_y\frac{(z+\gamma)^4}{d^2}} . \tag{17b}$$

The x, y-directions have the same form so we continue only with y. Eq. 13 requires the first and second derivatives $\frac{\partial \mu(x_k, y_k)}{\partial \theta_z}$ and $\frac{\partial^2 \mu(x_k, y_k)}{\partial \theta_z^2}$ to fit the z position. These are calculated from

$$\frac{\partial \mu(x_k, y_k)}{\partial \theta_z} = \frac{\partial \mu}{\partial \sigma_x} \frac{\partial \sigma_x}{\partial \theta_z} + \frac{\partial \mu}{\partial \sigma_y} \frac{\partial \sigma_y}{\partial \theta_z}, \tag{18a}$$

$$\frac{\partial^2 \mu(x_k, y_k)}{\partial \theta_z^2} = \frac{\partial^2 \mu}{\partial \sigma_x^2} \left(\frac{\partial \sigma_x}{\partial \theta_z} \right)^2 + \frac{\partial \mu}{\partial \sigma_x} \frac{\partial^2 \sigma_x}{\partial \theta_z^2} \tag{18b}$$

$$+ \frac{\partial^2 \mu}{\partial \sigma_y^2} \left(\frac{\partial \sigma_y}{\partial \theta_z} \right)^2 + \frac{\partial \mu}{\partial \sigma_y} \frac{\partial^2 \sigma_y}{\partial \theta_z^2}. \tag{18c}$$

The first and second derivatives σ_y to θ_z are given by

$$\frac{\partial \sigma_y}{\partial \theta_z} = \frac{\sigma_0 (\frac{2z}{d^2} + A\frac{3z^2}{d^2} + B\frac{4z^3}{d^2})}{2\sqrt{1 + \frac{z^2}{d^2} + A\frac{z^3}{d^2} + B\frac{z^4}{d^2}}}, \tag{19a}$$

$$\frac{\partial^2 \sigma_y}{\partial \theta_z^2} = \frac{\sigma_0 (\frac{2}{d^2} + A\frac{6z}{d^2} + B\frac{12z^2}{d^2})}{2\sqrt{1 + \frac{z^2}{d^2} + A\frac{z^3}{d^2} + B\frac{z^4}{d^2}}} - \frac{\sigma_0 (\frac{2z}{d^2} + A\frac{3z^2}{d^2} + B\frac{4z^3}{d^2})^2}{4(1 + \frac{z^2}{d^2} + A\frac{z^3}{d^2} + B\frac{z^4}{d^2})^{\frac{3}{2}}}. \tag{19b}$$

It does not matter for the result of the differentiation if the substitution $z \to z \pm \gamma$ is done before or after, so $\frac{\partial^2 \sigma_{x,y}}{\partial \theta_z^2}$ is obtained by substituting $z \to z \pm \gamma$ in the derivatives Eqs. 19b. Using the expressions

$$G_x^{nm}(x_k) \equiv \frac{1}{\sqrt{2\pi}\sigma_x(\theta_z)^n} \left((x_k - \theta_x - \frac{1}{2})^m e^{\frac{-(x_k - \theta_x - \frac{1}{2})^2}{2\sigma_x(\theta_z)^2}} - (x_k - \theta_y + \frac{1}{2})^m e^{\frac{-(x_k - \theta_y + \frac{1}{2})^2}{2\sigma_x(\theta_z)^2}} \right) \tag{20a}$$

$$G_y^{nm}(y_k) \equiv \frac{1}{\sqrt{2\pi}\sigma_y(\theta_z)^n} \left((y_k - \theta_y - \frac{1}{2})^m e^{\frac{-(y_k - \theta_y - \frac{1}{2})^2}{2\sigma_y(\theta_z)^2}} - (y_k - \theta_y + \frac{1}{2})^m e^{\frac{-(y_k - \theta_y + \frac{1}{2})^2}{2\sigma_y(\theta_z)^2}} \right) \tag{20b}$$

to shorten notation, we obtain for the derivatives of μ to σ_y

$$\frac{\partial \mu(x_k, y_k)}{\partial \sigma_y} = \theta_{I_0} \Delta E_x(x_k) G_y^{21}(y_k), \tag{21a}$$

$$\frac{\partial^2 \mu(x_k, y_k)}{\partial \sigma_y^2} = \theta_{I_0} \Delta E_x(x_k) (G_y^{53}(y_k) - 2G_y^{31}(y_k)). \tag{21b}$$

Supplementary Data

Performance on Synthetic Data Sets

Supplementary Fig. 6 shows the CRLB determined best accuracy as a function of a linear box size as well as the results from GPU fits. The results suggest a 'rule of thumb' fitting region size of $2 \times 3\sigma + 1$, which gives near optimal results while keeping computational time down and reducing the probability of including nearby emitters in the fitted region. All further results are shown with fits using this box size. This limit is a direct consequence of the fact that 99% of the volume of a Gaussian is enclosed within 3σ. Increasing the box size effectively only includes more background.

Supplementary Fig. 7 shows the convergence of the iterative algorithm for x-position, background and fluorophore intensity. The position estimate converges quickly, whereas the background and fluorophore rates, which are required for calculating the localization accuracy require nearly 10 iterations. The shown example is for $\sigma_{PSF} = 3$ and a box size of 19, which was found to require the most iterations for convergence of all parameter combinations. All subsequent analyses shown were the result of 10 iterations, independent of σ_{PSF} or fit region size. In **Supplementary Fig. 5** we show example images of simulated single molecules with emission and background rates (in photons) that corresponds with the $\sigma_{PSF}/2$ as discussed in the main text. We find that in all conditions, when the reported CRLB is less than $\sigma_{PSF}/2$ (here 0.5), the reported CRLB matches the theoretical position, and the routine achieves the CRLB.

13

Performance on Experimental Single Molecule Data

2D Imaging

Imaging of single Cy5 fluorescent molecules was used to demonstrate the performance of the iterative method under typical single molecule imaging conditions. Since the position, intensity and background rate were not known *a-priori*, we analyzed a set of single molecules that had a steady emission rate over at least one hundred continuous frames. The found standard deviation of the x-position was compared to the mean value of the reported x-dimension localization accuracy, which is calculated for each image that made up a single particle 'trajectory'. As can be seen in **Supplementary Fig. 8**, the reported accuracy gives a good estimate of the actual localization accuracy over a wide range of fluorophore intensities. The results also demonstrate that the Gaussian PSF and pure Poisson noise model with neglection of read noise are appropriate approximations for single molecule localization in two dimensions.

3D Astigmatic Imaging

With the found fit parameters on the calibration set (**Methods, Astigmatic Imaging Section**) a synthetic data series was generated using 1000 expected photons per frame for the fluorophore, and one expected background count per pixel per frame. 1000 frames for each z-position were generated and analyzed. **Supplementary Fig. 2** shows the fitting result of the iterative algorithm, which performs a simultaneous fit to x, y, z, and the emission and background rates. The z-position fits both achieve the CRLB value and the CRLB is correctly reported. For fits that include z-position estimates, 20 iterations of the routine were required for convergence.

An analysis of the experimental bead data is shown in **Supplementary Fig. 3** and **4**. In contrast to fitting simulated 3D data, and all 2D data, the fitting of experimental data does not reach the CRLB. This is attributed to the fact for the CRLB to be justified, the model must be correct.

In 3D imaging, the out-of-focus images are more prone to shape changes of the PSF due to aberrations such as coma and spherical aberration. Therefore, these images do not exactly match the simple astigmatic model. We note, however, that our algorithm does perform a fast MLE given this model, and, as shown with analysis of simulated data, if aberrations can by minimized or eliminated, our routine will also correctly report z-position accuracies. Small amounts of spherical aberration already give rise to a small asymmetry between the two focal lines. Misalignment of the cylinder lens by Δx with respect to optical axis of the tube lens has the effect of a shift of the center of mass of the spot and will result in two different σ_0 fits for x and y as observed in **Supplementary Fig. 1**. The focal line along the cylinder axis is then displaced by $\sim (f_{tub}/f_{cyl})\Delta x = (180/500)\Delta x = 0.36\Delta x$ which translates to a shift of $\sim 1/3$ pixel at a $\Delta x = 10\mu$m and a CCD pixel size of 10 μm.

If aberrations cannot be sufficiently reduced and alignment manually adjusted by a micrometer screw, optimal position precision may require fitting to a measured PSF [8], at the expense of speed.

References

[1] Hanser, B. M., Gustafsson, M. G. L., Agard, D. A. & Sedat, J. W. Phase-retrieved pupil functions in wide-field fluorescence microscopy. *Journal of Microscopy-Oxford* **216**, 32–48 (2004).

[2] Schönle, A. & Hell, S. Calculation of vectorial three-dimensional transfer functions in large angle focusing systems. *Journal of the Optical Society of America A* **19**, 2121–2126 (2002).

[3] Zhang, B., Zerubia, J. & Olivo-Marin, J. C. Gaussian approximations of fluorescence microscope point-spread function models. *Applied Optics* **46**, 1819–1829 (2007).

[4] NVIDIA. Compute unified device architecture (cuda) (2007). http://www.nvidia.com.

[5] Kay, S. M. *Fundamentals of statistical signal processing: estimation theory* (Prentice-Hall, 1993).

[6] Press, W., Teukolsky, S., Vetterling, W. & Flannery, B. *Numerical Recipes in C: The Art of Scientific Computing* (Cambridge University Press, Cambridge, 1992), 2 edn.

[7] Holtzer, L., Meckel, T. & Schmidt, T. Nanometric three-dimensional tracking of individual quantum dots in cells. *Applied Physics Letters* **90**, 1–3 (2007).

[8] Mlodzianoski, M. J., Juette, M. F., Beane, G. L. & Bewersdorf, J. Experimental characterization of 3d localization techniques for particle-tracking and super-resolution microscopy. *Optics Express* **17**, 8264–8277 (2009).